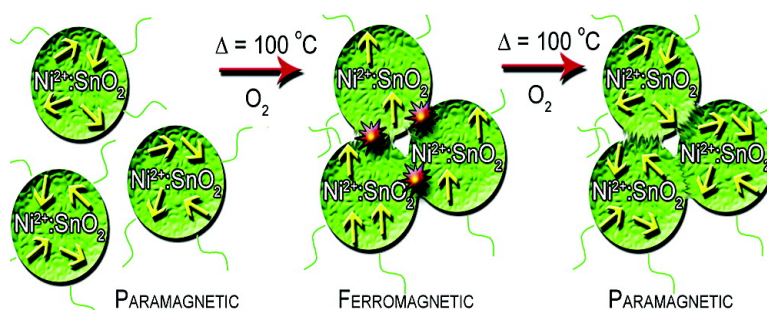Article

Low-Temperature Activation and Deactivation of High-Curie-Temperature Ferromagnetism in a New Diluted Magnetic Semiconductor: Ni-Doped SnO

Paul I. Archer, Pavle V. Radovanovic, Steve M. Heald, and Daniel R. Gamelin

More About This Article

Additional resources and features associated with this article are available within the HTML version:

- Supporting Information
- Links to the 7 articles that cite this article, as of the time of this article download
- Access to high resolution figures
- Links to articles and content related to this article
- Copyright permission to reproduce figures and/or text from this article

View the Full Text HTML

Low-Temperature Activation and Deactivation of High-Curie-Temperature Ferromagnetism in a New Diluted Magnetic Semiconductor: Ni²⁺-Doped SnO₂

Paul I. Archer,[†] Pavle V. Radovanovic,[†,‡] Steve M. Heald,[§] and Daniel R. Gamelin[*,†]

Contribution from the Department of Chemistry, University of Washington, Seattle, Washington 98195-1700, and Fundamental Science Directorate, Pacific Northwest National Laboratory, P.O. Box 999, MS K8-93, Richland, Washington 99352

Received June 24, 2005; E-mail: Gamelin@chem.washington.edu

Abstract: We report the synthesis of colloidal Ni²⁺-doped SnO₂ (Ni²⁺:SnO₂) nanocrystals and their characterization by electronic absorption, magnetic circular dichroism, X-ray absorption, magnetic susceptibility, scanning electron microscopy, and X-ray diffraction measurements. The Ni²⁺ dopants are found to occupy pseudooctahedral Sn⁴⁺ cation sites of rutile SnO₂ without local charge compensation. The paramagnetic nanocrystals exhibit robust high-Curie-temperature (T_C) ferromagnetism (M_s(300 K) = 0.8 μ_B/Ni²⁺, $T_C \gg$ 300 K) when spin-coated into films, attributed to the formation of interfacial fusion defects. Facile reversibility of the paramagnetic−ferromagnetic phase transition is also observed. This magnetic phase transition is studied as a function of temperature, time, and atmospheric composition, from which the barrier to ferromagnetic activation (E_a) is estimated to be 1200 cm⁻¹. This energy is associated with ligand mobility on the surfaces of the Ni²⁺:SnO₂ nanocrystals. The phase transition is reversed under air but not under N₂, from which the microscopic identity of the activating defect is proposed to be interfacial oxygen vacancies.

I. Introduction

The development of diluted magnetic semiconductors (DMSs)[1] as potential spin-based electronic, or spintronics, device components has garnered an increasing interest in the nanoscience community.[2] By use of electron spins in combination with charges, spintronics devices could potentially revolutionize information storage and transfer, reduce power consumption, and reduce hardware dimensions. To use DMSs for practical spintronics devices, they must exhibit ferromagnetic ordering at temperatures far above room temperature. Recent theoretical and experimental advances toward this goal have identified oxide DMSs as promising candidate materials for such applications.[3−6]

SnO₂ is an attractive host lattice for the investigation of DMS ferromagnetism because it is natively n-type because of oxygen vacancies, has a high carrier density, and has a structure similar to that of TiO₂, the lattice in which high-Curie-temperature (T_C) oxide DMS ferromagnetism was first discovered.[7] Because most DMS ferromagnetism is thought to involve electrons or holes mediating long-range communication between dopants,[3,5,6] the native oxygen vacancies and high carrier density of SnO₂ may render this lattice particularly conducive to applications requiring high-T_C ferromagnetism.[5,8] Recently, high-T_C ferromagnetism in Co²⁺:SnO₂ thin films grown by pulsed laser deposition was reported.[9] A subsequent study on similar thin films failed to verify this ferromagnetism, however, and only paramagnetism was observed.[10] Other reports have since appeared claiming

† University of Washington.
‡ Now at Department of Chemistry and Chemical Biology, Harvard University, 12 Oxford Street, Cambridge, MA 02138.
§ Pacific Northwest National Laboratory.

(1) Furdyna, J. K. *J. Appl. Phys.* **1988**, *64*, R29.
(2) Wolf, S. A.; Awschalom, D. D.; Buhrman, R. A.; Daughton, J. M.; von Molnár, S.; Roukes, M. L.; Chthelkanova, A. Y.; Treger, D. M. *Science* **2001**, *294*, 1488. Ohno, Y.; Young, D. K.; Beschoten, B.; Matsukura, F.; Ohno, H.; Awschalom, D. D. *Nature* **1999**, *402*, 790. Awschalom, D. D.; Flatté, M. E.; Samarth, N. *Sci. Am.* **2002**, *286*, 66. Fiederling, R.; Keim, M.; Reuscher, G.; Ossau, W.; Schmidt, G.; Waag, A.; Molenkamp, L. W. *Nature* **1999**, *402*, 787. Jonker, B. T.; Park, Y. D.; Bennett, B. R.; Cheong, H. D.; Kioseoglou, G.; Petrou, A. *Phys. Rev. B* **2000**, *62*, 8180. Rüster, C.; Borzenko, T.; Gould, C.; Schmidt, G.; Molenkamp, L. W.; Liu, X.; Wojtowicz, T. H.; Furdyna, J. K.; Yu, Z. G.; Flatté, M. E. *Phys. Rev. Lett.* **2003**, *91*, 216602/1. Chakrabarti, S.; Holub, M. A.; Bhattacharya, P.; Mishima, T. D.; Santos, M. B.; Johnson, M. B.; Blom, D. A. *Nano Lett.* **2005**, *5*, 209.
(3) Sato, K.; Katayama-Yoshida, H. *Physica E* **2001**, *10*, 251. Dietl, T.; Ohno, H.; Matsukura, F.; Cibert, J.; Ferrand, D. *Science* **2000**, *287*, 1019.
(4) Pearton, S. J.; Abernathy, C. R.; Overberg, M. E.; Thaler, G. T.; Norton, D. P.; Theodoropoulou, N.; Hebard, A. F.; Park, Y. D.; Ren, F.; Kim, J.; Boatner, L. A. *J. Appl. Phys.* **2003**, *93*, 1. Chambers, S. A.; Thevuthasan, S.; Farrow, R. F. C.; Marks, R. F.; Thiele, J. U.; Folks, L.; Samant, M. G.; Kellock, A. J.; Ruzycki, N.; Ederer, D. L.; Diebold, U. *Appl. Phys. Lett.* **2001**, *79*, 3467. Punnoose, A.; Hays, J.; Gopal, V.; Shutthanandan, V. *Appl. Phys. Lett.* **2004**, *85*, 1559.
(5) Coey, J. M. D.; Venkatesan, M.; Fitzgerald, C. B. *Nat. Mater.* **2005**, *4*, 173.
(6) Kittilstved, K. R.; Norberg, N. S.; Gamelin, D. R. *Phys. Rev. Lett.* **2005**, *94*, 147209/1.
(7) Matsumoto, Y.; Murakami, M.; Shono, T.; Hasegawa, T.; Fukumura, T.; Kawasaki, M.; Ahmet, P.; Chikyow, T.; Koshihara, S.; Koinuma, H. *Science* **2001**, *291*, 854.
(8) Rumyantseva, M. N.; Safonova, O. V.; Boulova, M. N.; Ryabova, L. I.; Gas'kov, A. M. *Russ. Chem. Bull.* **2003**, *52*, 1217.
(9) Ogale, S. B.; Choudhary, R. J.; Buban, J. P.; Lofland, S. E.; Shinde, S. R.; Kale, S. N.; Kulkarni, V. N.; Higgins, J.; Lanci, C.; Simpson, J. R.; Browning, N. D.; Das Sarma, S.; Drew, H. D.; Greene, R. L.; Venkatesan, T. *Phys. Rev. Lett.* **2003**, *91*, 077205/1.
(10) Fitzgerald, C. B.; Venkatesan, M.; Douvalis, A. P.; Huber, S.; Coey, J. M. D.; Bakas, T. *J. Appl. Phys.* **2004**, *95*, 7390.

some intrinsic ferromagnetism in vanadium-,[11] chromium-,[12] iron- (Fe^{3+}),[13] and manganese-doped[10] SnO_2 despite the apparent propensity for dopant phase segregation from this lattice.[14] The inconsistencies in the existing literature with respect to issues such as reproducibility of magnetic properties, dopant segregation, or inhomogeneous dopant speciation reflect the early stage of development of this field. Indeed, understanding the high-T_C ferromagnetism of oxide DMSs has been cited as among the most important new challenges in the field of magnetism.[5,15]

Understanding the magnetism of oxide DMSs is complicated by the critical roles apparently played by defects other than the magnetic dopant ions themselves.[6,16] In particular, there is a growing recognition of the importance of interfacial fusion defects in the activation of high-T_C ferromagnetism in oxide DMSs.[5,17,18] Ultimately, the microscopic origins of ferromagnetism in diluted magnetic oxides can only be described by concretely defining the roles of such defects using a combination of experimental and theoretical approaches. Attempts to describe the roles of defects theoretically have been hindered by the fact that many experimental issues remain too poorly defined for accurate detailed theoretical analysis. From the experimental standpoint, a suitable combination of synthetic approaches, dopant-specific and bulk physical probes, and well-designed control experiments must be employed to fully define the properties of these materials.

In this manuscript, we report the synthesis and physical properties of a new high-T_C ferromagnetic DMS, Ni^{2+}-doped SnO_2 (Ni^{2+}:SnO_2), prepared and processed by direct chemical methods entirely under mild oxidative conditions that preclude the segregation of ferromagnetic nickel metal or any other impurity phase. We describe the discovery that ferromagnetism in Ni^{2+}:SnO_2 can be activated and subsequently deactivated by extremely mild annealing under air, a phenomenon attributed to generation and quenching of oxygen vacancies at nanocrystal−nanocrystal fusion interfaces.

II. Experimental Section

A. Synthesis. Ni^{2+}:SnO_2 nanocrystals (NCs) were prepared by adapting a literature preparation developed to synthesize pure SnO_2 powder.[19] In a typical preparation, 1.400 g of $SnCl_4$·$5H_2O$, an appropriate amount of $NiCl_2$·$6H_2O$, and 5.000 g of Urea (Baker, 99%) were added to 100 mL of deionized water. HCl was added to ensure dissolution, and the precursors were stirred in air overnight at ca. 95 °C, during which time the Ni^{2+}:SnO_2 NCs formed. The precipitates were processed six times by washing with deionized water and centrifuging for several minutes until no chloride ions were detected in the supernatant after addition of $AgNO_3$.

We have previously shown that dopants on the NC surfaces can be removed, and the NCs can be resuspended in nonpolar solvents by heating in trioctylphosphine oxide (TOPO).[18,20] For TOPO treatment (Aldrich, tech grade) (1 g/mL of solution), the precipitated NCs were

suspended in melted dodecylamine (Aldrich, 98%) (DDA, mp ca. 30 °C) and heated under nitrogen at 150 °C for 30 min. The DDA-capped NCs were cooled to less than 80 °C, precipitated with ethanol, and resuspended in melted TOPO. The suspension was then heated under nitrogen at 150 °C for 1 h. Selective precipitation with ethanol followed by repeated TOPO cleaning and precipitation yielded TOPO-capped Ni^{2+}:SnO_2 NCs that were redispersed in a small amount of toluene. The transparent, light green, colloidal suspensions of high optical quality remained stable indefinitely, showing no visible signs of light scattering or precipitation over the course of several months. Dopant concentrations were measured by inductively coupled plasma atomic emission spectrometry (ICP−AES, Jarrel-Ash model 955) using elemental calibration standards (High Purity Standards). For quantitative magnetic measurements, the total nickel content was determined from the ICP-AES concentration and the mass of Ni^{2+}:SnO_2 measured after ligand calcination.

Nanocrystalline films of Ni^{2+}:SnO_2 were prepared for magnetic measurements by spin-coating the TOPO-capped Ni^{2+}:SnO_2 colloids onto fused silica substrates. For standard measurements, films were calcined aerobically at 350 °C for 1.5 min after each spin-coated layer was added. Approximately 10 layers were added in each film. The dependence of magnetization saturation on anneal temperature was conducted by annealing a spin-coated thin film prepared at room temperature under air for 1.5 min at each temperature. The dependence of magnetization saturation on anneal time was conducted by annealing a spin-coated film prepared at room temperature under air and inert (N_2) atmosphere for different time increments at 100 °C. In both sets of experiments, the heated films were rapidly cooled in the same atmosphere, weighed, and analyzed.

B. Physical Characterization. Absorption spectra were collected on a Cary 5E (Varian) spectrophotometer using 1 cm path-length quartz cuvettes. Magnetic circular dichroism (MCD) spectra were collected using a UV/visable/near-infrared (UV/vis/NIR) MCD instrument constructed from an AVIV 40DS spectropolarimeter and a high-field superconducting magnetooptical cryostat (Cryo-Industries SMC-1659 OVT) with a variable-temperature sample compartment positioned in the Faraday configuration. Magnetic circular dichroism samples were prepared by drop-coating the Ni^{2+}:SnO_2 colloids onto quartz disks to form frozen solutions. Magnetic susceptibilities were collected using a Quantum Design Magnetic Property Measurement System with a reciprocating sample option. All magnetic data were corrected for the diamagnetism of the substrate and sample holder.

Scanning electron microscopy (SEM) images were collected using a Scion XL-30 field emission microscope. X-ray diffraction (XRD) data were collected on a 12 kW Rigaku Rotoflex rotating anode diffractometer. XRD film was prepared at room temperature and annealed as described. Thermogravimetric analysis (TGA) was conducted on a TGA Q50 v6.1 Build 181 under air (40.0 mL/min) and a temperature ramp of 10.00 °C/min for the temperature-dependent anneal, and a ramp of 50 °C/min to 100 °C for the time-dependent anneal.

X-ray absorption measurements were made at the PNC-CAT beam line 20 μ_B at the advanced photon source (Argonne National Laboratory) using a Si(111) double-crystal monochromator with an energy resolution of ∼1.3 eV at the Ni edge. Beam harmonics were rejected using a rhodium-coated mirror at a 6 mrad incident angle. Ni fluorescence was detected using a 13-element Ge detector. Al foil (∼75 μm) was used to filter out the Sn fluorescence. A Ni foil was used to calibrate the energy, with the first peak in the first derivative in the edge set at 8331.5 eV. The film sample surface was oriented at approximately 2° to the beam to enhance the signal. The powder sample was mixed with a small amount of vacuum grease and packed into a 1 mm thick holder.

(11) Hong, N. H.; Sakai, J. *Physica B: Condens. Matter* **2005**, *358*, 265.
(12) Hong, N. H.; Sakai, J.; Prellier, W.; Hassini, A. *J. Phys.: Condens. Matter* **2005**, *17*, 1697.
(13) Coey, J. M. D.; Douvalis, A. P.; Fitzgerald, C. B.; Venkatesan, M. *Appl. Phys. Lett.* **2004**, *84*, 1332.
(14) Davis, S. R.; Chadwick, A. V.; Wright, J. D. *J. Mater. Chem.* **1998**, *8*, 2065. Davis, S. R.; Chadwick, A. V.; Wright, J. P. *J. Phys. Chem. B* **1997**, *101*, 9901.
(15) Dietl, T. *Nat. Mater.* **2003**, *2*, 646.
(16) Kittilstved, K. R.; Gamelin, D. R. *J. Am. Chem. Soc.* **2005**, *127*, 5292.
(17) Radovanovic, P. V.; Gamelin, D. R. *Phys. Rev. Lett.* **2003**, *91*, 157202/1.
(18) Bryan, J. D.; Heald, S. M.; Chambers, S. A.; Gamelin, D. R. *J. Am. Chem. Soc.* **2004**, *126*, 11640.
(19) Song, K. C.; Kang, Y. *Mater. Lett.* **2000**, *42*, 283.

(20) Schwartz, D. A.; Norberg, N. S.; Nguyen, Q. P.; Parker, J. M.; Gamelin, D. R. *J. Am. Chem. Soc.* **2003**, *125*, 13205.
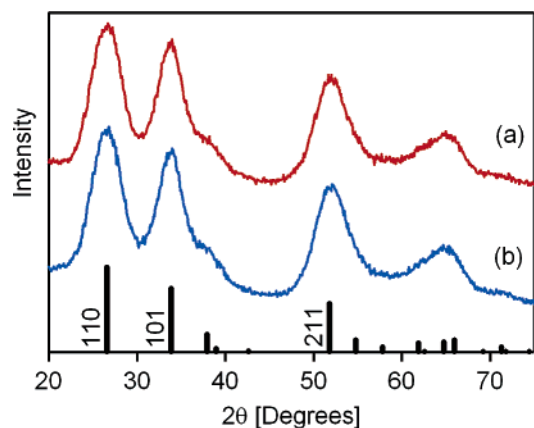
Figure 1. X-ray diffraction for a film of 0.39% Ni²⁺:SnO₂ before (a) and after (b) annealing at 100 °C for 11 min. Solid lines indicate the Bragg peak positions of bulk cassiterite SnO₂ for reference. NC diameter is approximately 3 nm.
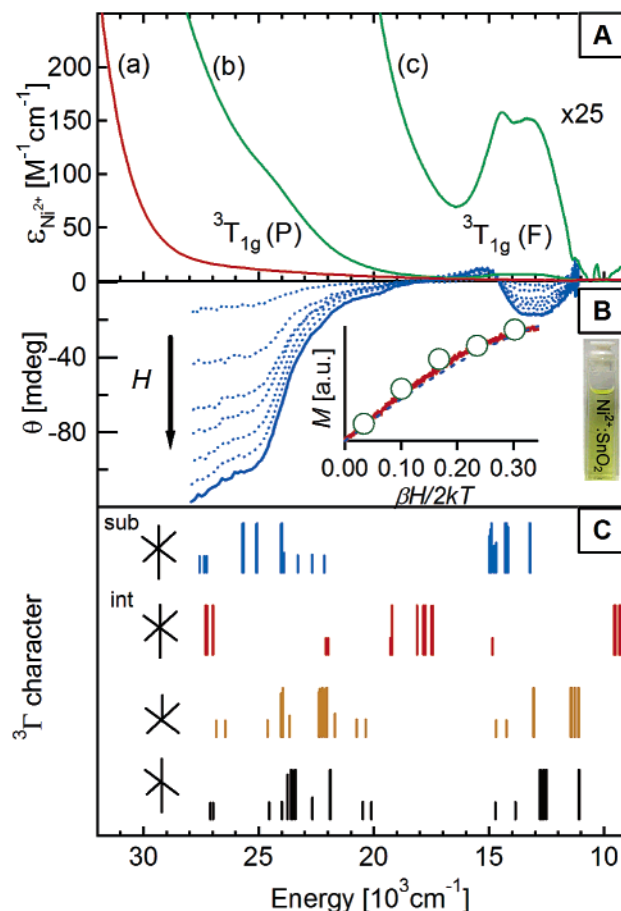
Thirty-eight scans were collected for each sample. XAS data analysis was performed as described previously.[21]

III. Results

Figure 1 shows powder X-ray diffraction (XRD) data collected for a film of ca. 3 nm diameter $0.39 \pm 0.02\%$ Ni²⁺: SnO₂ (i.e., Sn₀.₉₉₆Ni₀.₀₀₄O₂₋δ) nanocrystals deposited from toluene (a) before and (b) after annealing at 100 °C for 11 min. All peaks match those of bulk cassiterite SnO₂, as indicated by the indexed lines in the bottom of Figure 1, and no change was observed with annealing. SEM data collected for a spin-coated film calcined at 350 °C show uniform coverage with minor cracking (see Supporting Information Figure S1).

Electronic absorption spectra (300 K) of TOPO-capped SnO₂ (a) and $4.1 \pm 0.1\%$ Ni²⁺:SnO₂ (b and c) colloids suspended in toluene are presented in Figure 2A. The undoped SnO₂ NCs show only the band gap absorption onset at ca. 29 000 cm⁻¹ (~3.6 eV), in contrast to the green Ni²⁺-doped SnO₂ NCs, which show sub-band-gap features at 14 000 and 25 000 cm⁻¹, as well as a broad absorbance tail extending from the band gap into the visible region.

Figure 2B shows variable-field 5 K MCD spectra of the TOPO-capped 4.1% Ni²⁺:SnO₂ NCs. The spectra show a pseudo-𝒜-term feature associated with the absorption band at ~14 000 cm⁻¹ and a negative 𝒞-term feature at ~25 000 cm⁻¹ that coincides with the shoulder at the same energy in the absorption spectrum. The insets in Figure 2B show the 5 K MCD intensities probed at 13 661 (solid line) and 26 041 cm⁻¹ (circles) plotted as a function of the applied magnetic field, along with the spin-only $S = 1$ saturation curve approximated by the Brillouin function at 5 K (dashed line) and a photograph of the same colloids with lettering behind to illustrate the transparency of the suspension.[22] The indexed lines in Figure 2C represent the calculated ligand field transition energies of d⁸ Ni²⁺ in a pseudooctahedral (D_{2h} cation symmetry) environment with intensities represented by the ³Γ component of the wave function calculated by including spin−orbit coupling in the Hamiltonian (see section IV).

(21) Chambers, S. A.; Heald, S. M.; Droubay, T. *Phys. Rev. B* **2003**, *67*, 100401/1.
(22) Kittel, C. *Introduction to Solid State Physics*, 7th ed.; Wiley: New York, 1996.

Figure 2. (A) 300 K overview of absorption spectra: (a) colloidal TOPO-capped SnO₂ (undoped), (b) 4.1% Ni²⁺:SnO₂ NCs suspended in toluene, and (c) closeup of b. (B) Variable-field 5 K MCD spectra of a frozen solution of the doped NCs from b. Inset: 5 K MCD saturation magnetization probed at 13 661 (solid line) and 26 041 cm⁻¹ (circles). The dashed line shows the $S = 1$ spin-only saturation magnetization predicted by the Brillouin function (eq 1). Inset: photo of 4.1% Ni²⁺:SnO₂ NCs suspended in toluene with lettering behind it to illustrate the transparency. (C) Ligand field transition energies calculated for six-coordinate substitutional (sub) and interstitial (int) and five-coordinate (vacancy at axial or equatorial site) Ni²⁺ in SnO₂, as illustrated.
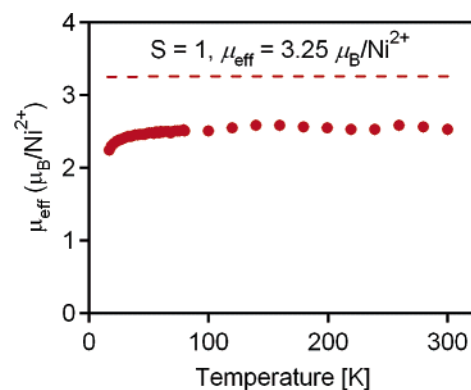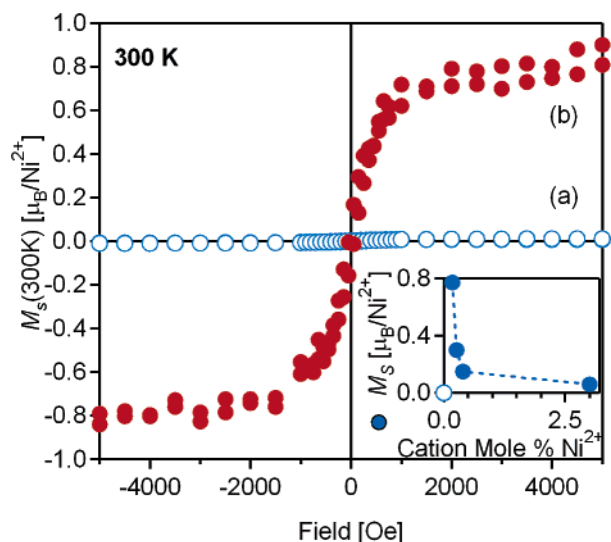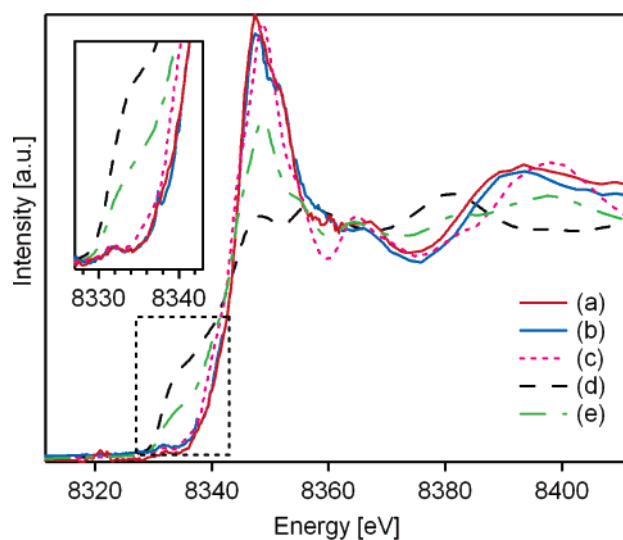

Figure 3. Temperature dependence of the effective magnetic moment (μ_{eff}) of 0.39% Ni²⁺:SnO₂ NCs. $H = 5000$ Oe. The dashed line shows the anticipated μ_{eff} for octahedral Ni²⁺ (see text for details).

Variable-temperature magnetic susceptibility data collected on 0.39% Ni²⁺:SnO₂ NCs are shown in Figure 3, plotted as the effective magnetic moment ($\mu_{eff} = 2.828\sqrt{\chi T}$) vs the temperature. μ_{eff} is temperature independent between 100 and 300 K, having a value of $\mu_{eff} = 2.55$ μ_B/Ni²⁺.

Figure 4. 300 K magnetization of (a) TOPO-capped 0.17% Ni^{2+}:SnO$_2$ NCs and (b) a spin-coated film of the same, calcined at 350 °C. All data have been corrected for a diamagnetic background. Inset: 300 K ferromagnetic saturation moments of spin-coated films of Ni^{2+}:SnO$_2$ at varying Ni^{2+} concentrations.

Figure 5. Nickel K-shell X-ray absorption spectra of (a) precipitated 0.26% Ni^{2+}:SnO$_2$ colloids, (b) a spin-coated film of 0.26% Ni^{2+}:SnO$_2$ annealed aerobically at 300 °C (M_s(300 K) ~ 0.3 μ_B/Ni^{2+}), (c) a Ni^{2+} reference, NiO, and (d) Ni metal foil. (e) Simulated spectrum for a Ni metal/NiO blend that would yield the same ferromagnetism as observed in the Ni^{2+}:SnO$_2$ film (spectrum b).

Figure 4 presents the 300 K magnetic susceptibilities (a) of a 0.17 ± 0.07% Ni^{2+}:SnO$_2$ powder precipitated rapidly from toluene by addition of ethanol and (b) of a representative film prepared by spin-coating the same 0.17% Ni^{2+}:SnO$_2$ NCs onto fused silica with calcination at 350 °C. Whereas paramagnetism dominates the magnetism of the powder sample resulting in little detectable magnetization at 300 K, strong ferromagnetic ordering is observed in the spin-coated film, with a rapid ferromagnetic saturation moment (M_s(300 K) = 0.8 μ_B/Ni^{2+}) and a 300 K coercivity (H_c) of 100 Oe. The maximum spin-only saturation moment of Ni^{2+} is 2.0 μ_B/Ni^{2+}. Control experiments in which films were spin-coated from undoped TOPO-capped SnO$_2$ colloids yielded only diamagnetism (not shown), indicating that the ferromagnetism is indeed due to the Ni^{2+} dopants. The ferromagnetism is relatively temperature independent between 2 and 300 K (Supporting Information Figure S2).
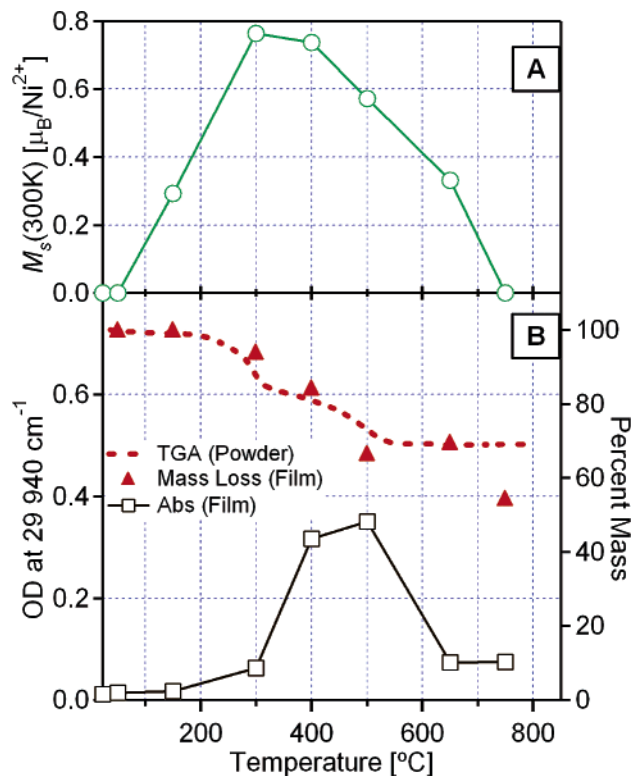
The inset to Figure 4 shows the dependence of the Ni^{2+}: SnO$_2$ 300 K ferromagnetic saturation moment on the Ni^{2+} concentration for a series of films, plotted as μ_B/Ni^{2+}. There is no ferromagnetism in spin-coated films of undoped SnO$_2$ (open circle, in emu/g). The ferromagnetism reaches a maximum of M_s(300 K) = 0.8 μ_B/Ni^{2+} at 0.17% Ni^{2+}, decreases rapidly at 0.39% Ni^{2+} (M_s(300 K) = 0.15 μ_B/Ni^{2+}), and levels out at higher Ni^{2+}-dopant concentrations.

Figure 5 shows nickel K-shell X-ray absorption spectra of (a) the paramagnetic 0.26 ± 0.01% Ni^{2+}:SnO$_2$ NCs, (b) a ferromagnetic (M_s(300 K) ~ 0.3 μ_B/Ni^{2+}) spin-coated film of the same, (c) a Ni^{2+} reference, NiO, and (d) Ni metal foil. The Ni K-edge spectra of a and b are nearly identical, showing a sharp 1s → 4p transition edge at 8334.3 eV and a 1s → 3d preedge feature at 8331.5 eV (Figure 5 inset). Spectrum e represents a weighted average of the Ni metal and NiO spectra based on the experimental magnetic saturation of the film (see section IV).

Figure 6A shows the ferromagnetic saturation moment of a single spin-coated film of TOPO-capped 0.26% Ni^{2+}:SnO$_2$ NCs prepared with no annealing and collected as a function of aerobic annealing temperature. Prior to annealing, the film showed no
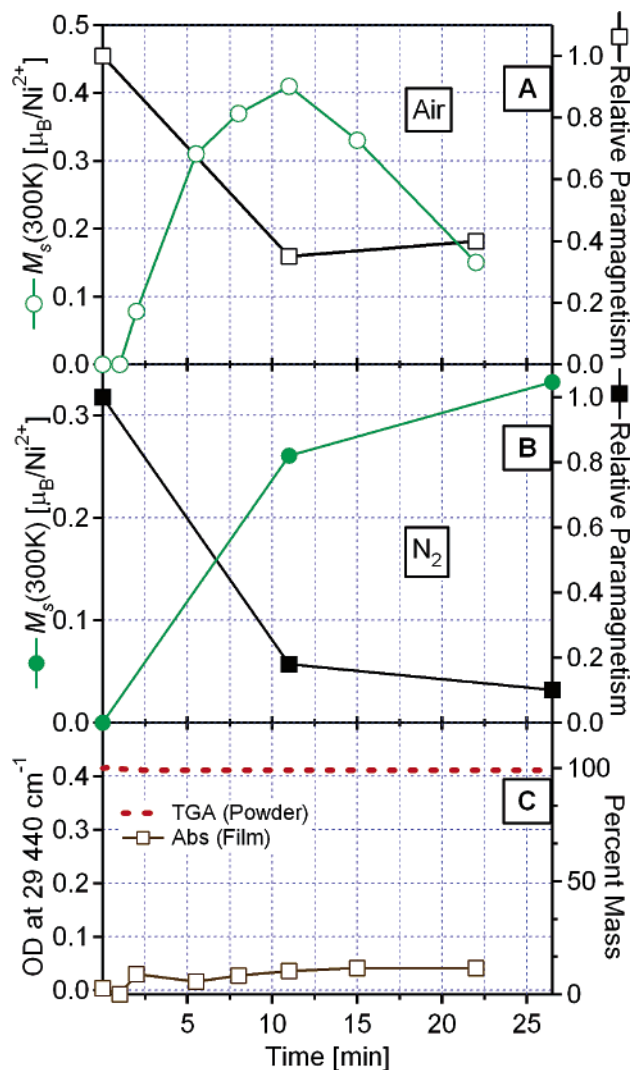
Figure 6. (A) 300 K ferromagnetic saturation moment of a spin-coated film of TOPO-capped 0.26% Ni^{2+}:SnO$_2$ NCs, measured as a function of annealing temperature. (B) TGA data for TOPO-capped Ni^{2+}:SnO$_2$ NC powder and weight loss and optical density of the film from part A, monitored at 29 940 cm^{-1} as a function of temperature. Film weight loss was corrected for substrate weight loss.

ferromagnetism. The ferromagnetic saturation moment reached a maximum of M_s(300 K) ~ 0.78 μ_B/Ni^{2+} with annealing at 300 °C and decreased to zero when the temperature was raised to 750 °C. Figure 6B shows the change in mass of the same film (triangles), plotted with the TGA curve collected on Ni^{2+}: SnO$_2$ powder (solid line). In both curves of Figure 6B, an initial

Figure 7. (A) 300 K ferromagnetic saturation moment and relative paramagnetism of a spin-coated film of TOPO-capped 0.48% Ni^{2+}:SnO_2 NCs prepared without any annealing. Data were collected as a function of aerobic annealing time at 100 °C. (B) 300 K ferromagnetic saturation moment of a spin-coated film of Ni^{2+}:SnO_2 and relative paramagnetism as a function of annealing time under inert (N_2) atmosphere at 100 °C. (C) TGA data for TOPO-capped Ni^{2+}:SnO_2 NC powder and optical density of a spin-coated film monitored at 29 940 cm^{-1} as a function of annealing time under the conditions of part A. The 0.05 OD offset observed is due to scattering.

low-temperature plateau is followed by a steady loss of mass from 250 to 500 °C and then a relatively constant mass above 500 °C. Upon aerobic calcination, the films exhibited a brown color. The 300 K optical density (OD) of the same film was monitored at 29 940 cm^{-1}, and the results are also displayed in Figure 6B. The OD increased to a maximum of 0.35 absorbance units with annealing at 500 °C and then decreased at elevated temperatures.

Figure 7A shows the 300 K ferromagnetic saturation moment (M_s(300 K)) of a spin-coated film of TOPO-capped 0.48 ± 0.08% Ni^{2+}:SnO_2 NCs prepared without any annealing and the relative 10 K paramagnetism (normalized to zero anneal time) of a second film from the same batch, collected as a function of aerobic annealing time at a temperature of only 100 °C. Initially, the films showed only paramagnetism and no ferromagnetism. With increased annealing time, the relative para-

magnetism decreased to ~35% as the ferromagnetism increased, reaching a maximum of M_s(300 K) ~ 0.41 μ_B/Ni^{2+} at 11 min. With further annealing at 100 °C, the relative paramagnetism increased to ~40% of the initial value and the ferromagnetism decreased to M_s(300 K) ~ 0.15 μ_B/Ni^{2+}. Figure 7B shows the ferromagnetic saturation moment of a spin-coated film (prepared as for Figure 7A) of a second batch of TOPO-capped 0.40% Ni^{2+}:SnO_2 NCs and the relative paramagnetism collected as a function of annealing time at 100 °C under a nitrogen atmosphere. The ferromagnetism reached a maximum of M_s-(300 K) ~ 0.33 μ_B/Ni^{2+}, and the relative paramagnetism decreased to ~10% after 26.5 min at 100 °C. Figure 7C shows the TGA curve collected on the same NCs as a function of annealing time at 100 °C. Over the course of 25 min, less than 0.1% mass was lost. The OD, presented in Figure 7C, was also monitored, as in Figure 6B, and remained below 0.05 absorbance units over the entire annealing time period.

IV. Analysis and Discussion

A. Characterization of Paramagnetic Ni^{2+}:SnO_2. To verify the successful synthesis of Ni^{2+}:SnO_2, the synthetic product was carefully characterized by structural, spectroscopic, and magnetic techniques.

(i) Crystallographic Characterization. All of the peaks observed in the XRD data (Figure 1) for the nanocrystalline film before and after aerobic annealing at 100 °C for 11 min match those of rutile cassiterite SnO_2, with no detectable impurity phases. Analysis of the 110, 101, and 211 peak widths using the Debye–Scherrer equation[23] yielded an average grain diameter of ca. 3 nm for both samples, indicating no substantial increase in crystal grain size with low-temperature annealing. This average grain diameter is consistent with that anticipated from the related preparation of pure SnO_2 NCs from which our synthesis was adapted.[19]

(ii) Ni^{2+} Coordination Environment. To characterize the DMS properly, dopant speciation must be determined, and this requires use of dopant-specific physical techniques. The absorption and MCD spectra of the Ni^{2+}:SnO_2 colloids show two distinct features in addition to the band gap absorption of SnO_2, which is responsible for the rising absorbance at ~29 000 cm^{-1} (Figure 2).[24] The band centered at 13 750 cm^{-1} is readily identified as the $^3A_{2g} \rightarrow {}^3T_{1g}$(F) ligand field transition, and the shoulder at ca. 25 000 cm^{-1} is identified as the $^3A_{2g} \rightarrow {}^3T_{1g}$(P) transition of a pseudooctahedral Ni^{2+} ion in a hexa-oxo coordination environment.[25] The Ni^{2+} molar extinction coefficients ($\epsilon_{13755} = 5.9$ and $\epsilon_{24213} = 10.9$ M^{-1} cm^{-1}) of the two ligand field bands correspond well with those of $Ni(H_2O)_6^{2+}$ ($\epsilon_{14500} = 2.0$ and $\epsilon_{25300} = 4.6$ M^{-1} cm^{-1}). Similar energies and band shapes are also observed in $Ni(H_2O)_6^{2+}$ (14 500 and 25 300 cm^{-1})[26] and Ni^{2+}:MgO (14 800 and 24 500 cm^{-1}),[27] although the transitions observed in the Ni^{2+}:SnO_2 NCs are shifted to lower energies relative to those of $Ni(H_2O)_6^{2+}$. This shift indicates a smaller effective ligand field strength of the lattice

(23) West, A. R. *Solid State Chemistry*; Wiley: Chichester, U.K., 1992.
(24) To higher energies, a broad absorption tail extends from the band edge into the visible region that is not present in undoped SnO_2 NCs. This band is tentatively assigned as a ligand–metal charge transfer (LMCT) transition involving partial transfer of a valence band electron to Ni^{2+} on the basis of optical electronegativity considerations.
(25) Brussiere, G.; Reber, C. *J. Am. Chem. Soc.* **1998**, *120*, 6306.
(26) Figgis, B. N.; Hitchman, M. A. *Ligand Field Theory and its Applications*; Wiley: New York, 2000; and references therein.
(27) Low, W. *Phys. Rev.* **1958**, *109*, 247.

Scheme 1
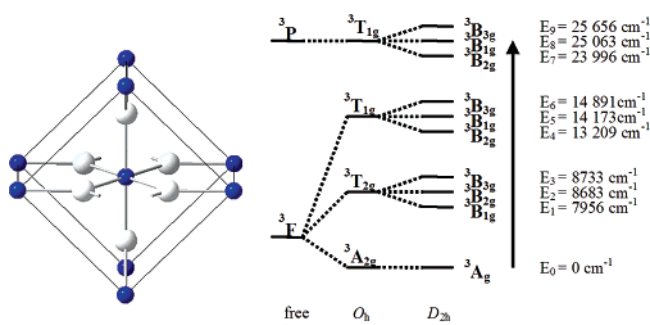
oxos in SnO_2 relative to that of water. The observation of only the $^3T_{1g}(F)$ and $^3T_{1g}(P)$ ligand field bands and the absence of other ligand field absorption bands allow the conclusion that all of the Ni^{2+} resides in a similar six-coordinate pseudooctahedral ligand field environment.

The similar sizes and geometries of the pseudooctahedral substitutional and interstitial cation sites in SnO_2 present the possibility that both locations could be potential Ni^{2+} doping sites.[28] To explore this possibility, ligand field transition energies for Ni^{2+}:SnO_2 were calculated[29] using ligand field parameters extrapolated from those of $Ni(H_2O)_6^{2+}$ ($Dq = 870$ cm^{-1}, $B = 900$ cm^{-1}, $C = 4.5B$)[26] and the spin–orbit coupling parameter, $\lambda = -245$ cm^{-1}, by approximating the lattice oxos as pure σ donors (i.e., $\Delta = 3e_\sigma$) and scaling the σ bond interaction with the M–L bond length ($Dq \propto a^{-5}$). Using the appropriate modified geometries,[28,30] we calculated the Ni^{2+} ligand field excited-state energies and wave functions for substitutional and interstitial Ni^{2+} dopants. With no fitting, the calculated energies for the substitutional Ni^{2+} geometry are in excellent agreement with the experimental results (Figure 2C) and match significantly better than those for Ni^{2+} in the interstitial geometry. In particular, the contracted axial bond lengths of the interstitial site give rise to a large $^3T_{1g}$ splitting that would place a spin-allowed band at 18 000 cm^{-1}, but the MCD and electronic absorption show no evidence of any transitions other than those at 14 000 and 25 000 cm^{-1}. Ligand field transition energies were also calculated for five-coordinate Ni^{2+} geometries on the basis of the consideration of possible charge compensation by the presence of an oxygen vacancy in the first coordination sphere of Ni^{2+}. Energies were calculated for vacancies in the axial and equatorial positions of the Ni^{2+} coordination sphere (Figure 2C). In both five-coordinate geometries, the calculated and observed transition energies are not in good agreement, suggesting that there are no five-coordinate Ni^{2+} ions in SnO_2. We note additionally that the molar extinction coefficients of the ligand field bands are also inconsistent with a five-coordinate geometry because the lack of inversion symmetry would yield molar absorptivities 2 or 3 orders of magnitude larger than those for six-coordinate species having inversion symmetry.[31]

The substitutional cation site symmetry in SnO_2 is reduced from O_h to D_{2h}, as depicted in Scheme 1 (dark spheres = Sn^{4+} and light spheres = O^{2-}). Axial bond contraction and deviation of the equatorial O–Sn–O angles from 90° to ~78.77° and

(28) Kilic, C.; Zunger, A. *Phys. Rev. Lett.* **2002**, *88*, 095501.
(29) Bendix, J. *LIGFIELD*, version 0.92x; Copenhagen, Denmark, 2004.
(30) West, A. R.; Bruce, P. G. *Acta Crystallogr.* **1982**, *B38*, 1891.
(31) Sacconi, L.; Bertini, I. *J. Am. Chem. Soc.* **1968**, *90*, 5443. Venanzi, L. M.; Dawson, J. W.; Preer, J. R.; Hix, J. E., Jr.; Gray, H. B. *J. Am. Chem. Soc.* **1971**, *93*, 778.

101.23° completely remove the O_h t_{2g} and e_g d-orbital degeneracies. The increased axial and decreased equatorial M–L bond lengths destabilize d_{z^2} relative to $d_{x^2-y^2}$, whereas the equatorial distortion destabilizes d_{xy} relative to d_{xz} and d_{yz} because of increased overlap. This reduced symmetry splits the $^3T_{1g}$ and $^3T_{2g}$ O_h excited states into $^3B_{1g}$, $^3B_{2g}$, and $^3B_{3g}$ terms (Scheme 1).[32] Second-order spin–orbit coupling within the low-symmetry split $^3T_{1g}$ term then gives rise to the pseudo-$\mathcal{A}$-term MCD feature at 14 000 cm^{-1}.

On the basis of the assignments and analysis of the Ni^{2+} ligand field transitions observed in Figure 2, we conclude that all of the Ni^{2+} ions occupy substitutional cationic sites of the SnO_2 NCs. This conclusion is supported by nickel K-edge X-ray absorption spectra (XAS) of the Ni^{2+}:SnO_2 NCs and films, which show a weak 1s → 3d preedge feature (Figure 5 inset) consistent with six-coordinate substitutional Ni^{2+} in SnO_2. In NiO, for example, the Ni^{2+} site has crystallographic inversion symmetry, and consequently, the 1s → 3d transition is rigorously Laporte forbidden, gaining only limited intensity through 3d–4p mixing. The very similar Ni^{2+} 1s → 3d preedge intensities of Ni^{2+}:SnO_2 and NiO therefore provide strong evidence that Ni^{2+} has inversion symmetry in SnO_2 as well. A much greater preedge intensity would be observed for five-coordinate Ni^{2+} geometries lacking an inversion center.[33] The nickel K-edge preedge absorption data fortify the conclusion drawn from analysis of the ligand field absorption spectra that charge compensation in Ni^{2+}:SnO_2 does not involve formation of an oxygen vacancy in the first coordination sphere of Ni^{2+}.

On the basis of the ligand field and XAS analysis, we conclude that dilute Ni^{2+} dopants in SnO_2 substitute for Sn^{4+} in distorted, six-coordinate D_{2h} geometries in the internal volumes of the SnO_2 NC lattices. The absorption, MCD, and XAS data all indicate that charge compensation in Ni^{2+}:SnO_2 does not involve the loss of a coordinating oxygen, which we attribute to the large ligand field stabilization energy of octahedral Ni^{2+}. Charge compensation must therefore be distal and not local. Possibilities include oxygen vacancies that are not localized in the Ni^{2+} coordination sphere (e.g., at the NC surfaces) or charge-balancing interstitial Sn^{4+}.

(iii) Magnetism. The inset in Figure 2B shows the 5 K MCD saturation magnetization probed at 13 661 (dashed line) and 26 401 cm^{-1} (circles) along with the spin-only saturation magnetization anticipated from the Brillouin function (eq 1),[22]

$$M = \frac{1}{2}Ng\mu_B\left[(2S+1)\coth\left((2S+1)\left(\frac{g\mu_BH}{2kT}\right)\right) - \coth\left(\frac{g\mu_BH}{2kT}\right)\right] \quad (1)$$

calculated using $g = 2.227$ from Ni^{2+}:MgO[27] and $S = 1$. The predicted and experimental curves agree well, demonstrating that these MCD intensities arise from an $S = 1$ chromophore and therefore from magnetically isolated d^8 Ni^{2+} ions.

More quantitatively, the experimental effective magnetic moment ($\mu_{eff} = 2.828\sqrt{\chi T}$) of the 0.39% Ni^{2+}:SnO_2 NCs shown in Figure 3 is temperature independent between 100 and 300 K with a value of $\mu_{eff} = 2.55$ μ_B/Ni^{2+}. Fitting the downturn

(32) Wilson, E. B.; Decius, J. C.; Cross, P. C. *Molecular Vibrations*; McGraw-Hill: New York, 1955.
(33) Randall, C. R.; Shu, L.; Chiou, Y.-M.; Hagen, K. S.; Ito, M.; Kitajima, N.; Lachicotte, R. J.; Zang, Y.; Que, L., Jr. *Inorg. Chem.* **1995**, *34*, 1036.

in μ_{eff} below 40 K yields a small positive Weiss constant of Θ = 5.8 K (from $\chi = C/(T - \Theta)$), consistent with a dilute magnetic material. The high-temperature value of μ_{eff} is lower than the octahedral, spin-only effective magnetic moment of Ni^{2+} ($\mu_{eff}^{s.o.} = g\sqrt{S(S+1)} = 2.83\ \mu_B/Ni^{2+}$) calculated using $g = 2.00$. This difference cannot be explained by a single-ion mechanism. Indeed, inclusion of orbital contributions to μ_{eff} reveals an even more substantial difference between experimental and predicted values. Using the calculated ligand field splitting energies (Δ), $\xi = 630\ cm^{-1}$ (for free ion Ni^{2+}), and assuming $k \approx 1$, we anticipate three g-values of ~ 2.30 for Ni^{2+}:SnO₂.[34] These values are nearly isotropic and may therefore be approximated collectively by eq 2. Importantly, each g-value is greater than 2.00

$$g_{iso} = 2.0023 - \frac{8\lambda k_{iso}^2}{\Delta} \tag{2}$$

because λ is negative for the d⁸ configuration ($\lambda = -\xi/2S$). Using the isotropic g-value of 2.30 calculated from eq 2 and the ligand field parameters given above, we estimate that μ_{eff} = 3.25 μ_B/Ni^{2+}. g-Value deviation from the spin-only value therefore cannot explain the low experimental μ_{eff} in Figure 3.

The reduction in μ_{eff} from 3.25 μ_B/Ni^{2+} to 2.55 μ_B/Ni^{2+} ($\sim 22\%$) observed experimentally is also too great to be explained by statistical dimer formation (only $\sim 3.7\%$ dimers formed at 0.39% Ni^{2+}).[35] We therefore tentatively attribute the reduced μ_{eff} to a small superstatistical preference for dimer formation driven by charge compensation, analogous to that observed in Ln^{3+}:CsCdCl₃.[36] In such a scenario, charge compensation could be achieved with two Ni^{2+} dopants and one interstitial Sn^{4+} substituting for two neighboring Sn^{4+} ions, leading to $Ni^{2+}-O-Ni^{2+}$ antiferromagnetic superexchange and a decreased μ_{eff}. The small superstatistical fraction of magnetically silent Ni^{2+} suggests that this mechanism for charge compensation is not the primary one.

B. Characterization of Ferromagnetic Ni^{2+}:SnO₂. When the Ni^{2+}:SnO₂ NCs are spin-coated into films and calcined aerobically at 350 °C, robust ferromagnetism is observed having a Curie temperature well above 300 K (Figure 4 and Supporting Information Figure S2) with a large 300 K saturation moment of $M_s = 0.8\ \mu_B/Ni^{2+}$ (compared to the maximum of 2.0 μ_B/Ni^{2+}) that exceeds the saturation moment of nickel metal, $M_s = 0.6\ \mu_B/Ni^{2+}$. To our knowledge, this high-T_C ferromagnetism is the first reported to date for Ni^{2+}-doped SnO₂. The very high Curie temperature ($T_C \gg 350$ K) implicated by these data is similar to those reported for other oxide DMSs.[5,16] Ferromagnetism in Ni^{2+}:SnO₂ is observed for a wide range of Ni^{2+} concentrations, ranging from 0.17% to 3.0% Ni^{2+} (Figure 4, inset), with a concentration dependence also similar to those reported for other oxide DMSs.[5,16]

Although the oxidative spin-coating conditions preclude the segregation of nickel metal, which would also show ferromagnetism, XAS was conducted to probe the nickel oxidation state and coordination environment in the ferromagnetic phase (Figure 5). The XAS spectra of Ni^{2+}:SnO₂ NCs and a calcined

ferromagnetic (M_s(300 K) $\sim$ 0.3 μ_B/Ni^{2+}) film are both very similar to that of the NiO reference, and all three spectra differ substantially from that of Ni metal. In particular, all three oxide samples lack the distinct shoulder at 8334 eV observed for Ni metal. For comparison, a reference spectrum was simulated using the weighted average of the NiO and Ni foil spectra that would yield the same magnitude of ferromagnetism as that measured in the Ni^{2+}:SnO₂ film. On the basis of the ferromagnetic saturation moment of nickel metal (M_s(300 K) = 0.6 μ_B/Ni) and that of the Ni^{2+}:SnO₂ film (M_s(300 K) $\sim$ 0.3 μ_B/Ni^{2+}), 50% of the nickel in the Ni^{2+}:SnO₂ film would have to be Ni^0 if the ferromagnetism were to arise from metallic precipitates. The resulting simulated spectrum (50% Ni^0 + 50% Ni^{2+}:SnO₂) is shown in the inset of Figure 5. The Ni^0 preedge shoulder is clearly observable in the simulated spectrum but is not observed in the spectra of either the NCs or the ferromagnetic film. From this analysis, we conclude that the ferromagnetism in Figure 4 arises from the DMS Ni^{2+}:SnO₂ and not from Ni^0. The similarity of the XAS data for the ferromagnetic film to those of paramagnetic Ni^{2+}:SnO₂ indicates that there is no significant difference in the Ni^{2+} coordination geometry or oxidation state between the two and, hence, that the activation of ferromagnetism does not involve a change in Ni^{2+} speciation. Nickel in the ferromagnetic phase remains Ni^{2+} octahedrally coordinated at the Sn^{4+} site of SnO₂. This conclusion is verified unambiguously by the low-temperature activation experiments described in section IV.C.

C. Low-Temperature Activation of Ferromagnetism in Ni^{2+}:SnO₂. As a first approach to identifying high-T_C ferromagnetism in Ni^{2+}:SnO₂, nanocrystalline thin films were prepared by spin-coat processing and calcination following the methodology found previously to be successful in generating strong ferromagnetism with other oxide DMSs.[18,37] In the course of these experiments, it became apparent that the 300 K ferromagnetic saturation moments of spin-coated Ni^{2+}:SnO₂ films annealed at 350 °C were significantly greater than those of films annealed at 500 °C. This peculiarity prompted a systematic investigation of the dependence of ferromagnetism on the annealing process. Two sets of experiments were performed to address this issue.

In the first set of experiments, a single spin-coated film of 0.26% Ni^{2+}:SnO₂ prepared at room temperature without any annealing was annealed aerobically for 1.5 min at a series of temperatures up to 750 °C. In addition to the measurement of the ferromagnetic saturation moment after each anneal, the film was weighed and analyzed optically to monitor TOPO calcination (Figure 6). With annealing temperatures up to 500 °C, the increase in ferromagnetism from 0 to 0.78 μ_B/Ni^{2+} was accompanied by a gradual loss of mass and an increase in brown color (Figure 6B), indicative of TOPO calcination. At annealing temperatures above 500 °C, after the TOPO was completely calcined, the ferromagnetism started to decrease. Two regimes (increase and decrease) are evident in these data and are interpreted as the activation and deactivation of ferromagnetism. We hypothesized that ferromagnetism may be activated by ligand calcination (which could reduce the lattice during formation of CO_2, for example). This hypothesis was quickly disproved by the second set of annealing experiments.

(34) Mabbs, F. E.; Collison, D. *Electron Paramagnetic Resonance of d Transition Metal Compounds*; Elsevier Science Publishers: Amsterdam, 1992; and references therein.
(35) Bryan, J. D.; Gamelin, D. R. *Prog. Inorg. Chem.* **2005**, *54*, 47.
(36) McPherson, G. L.; Henling, L. M. *Phys. Rev. B* **1977**, *16*, 1889. Henling, L. M.; McPherson, G. L. *Phys. Rev. B* **1977**, *16*, 4756. Jana, S.; Mukherjee, R. K. *Solid State Commun.* **2000**, *116*, 581.
(37) Schwartz, D. A.; Kittilstved, K. R.; Gamelin, D. R. *Appl. Phys. Lett.* **2004**, *85*, 1395.

In the second set of experiments, a film of 0.48% Ni^{2+}:SnO_2 prepared at room temperature without any annealing was annealed at 100 °C for various durations (Figure 7). Under these conditions, 300 K ferromagnetism was found to be activated and then slowly quenched during the course of the annealing (Figure 7A). The activation of ferromagnetism at such low temperatures rules out contributions from ligand calcination, as verified by the constant mass in the TGA curve and the absence of a brown color in the film (Figure 7C). This result also allows the conclusion that the variable-temperature activation of Ni^{2+}:SnO_2 ferromagnetism observed in Figure 6 is not dependent on ligand calcination at all, as already suggested by the increase in magnetic ordering (0−0.3 μ_B/Ni^{2+}) observed at ∼200 °C, before the onset of TOPO calcination. Equally important is the clear demonstration that ferromagnetism can be activated without any change in dopant speciation. This conclusion is based on the following observations: (i) this annealing temperature (100 °C) is below the surface-capping temperature used to prepare the colloidal NCs (150 °C), (ii) the ferromagnetism is activated over a much shorter time period than that used for surface capping (11 min vs 2.5 h), and (iii) the material returns to its paramagnetic phase with continued heating at 100 °C (Figure 7A squares).

We interpret the low-temperature activation of ferromagnetism in Figures 6 and 7 as arising from NC−NC aggregation, as described originally in Ni^{2+}:ZnO.[17] Direct evidence of irreversible NC−NC fusion comes from the observation that the nanocrystals of as-prepared spin-coated films (as in Figure 7) are readily resuspended in toluene but are no longer resuspendable after annealing at 100 °C for 10 min. A simple Arrhenius analysis of the rates of appearance of ferromagnetism with annealing at temperatures below 200 °C yields an estimated thermal activation energy of only ∼1200 cm^{-1}. It is emphasized that this activation barrier is not intrinsic to the internal lattice structure of Ni^{2+}:SnO_2 because the NCs have already been heated to 150 °C for 2.5 h during preparation but remained paramagnetic (Figures 3 and 4). This distinction rules out migration of charge compensating defects or dopants as the important thermally activated processes, for example. The facile reversibility of the magnetic phase transition (Figure 7) supports the conclusion that it is not accompanied by any structural rearrangement of the lattice (e.g., phase segregation, defect migration, or structural phase transition). Instead, we associate the thermal activation barrier with surface ligand mobility.

At 25 °C, the surface-capping ligands are effective in preventing NC−NC aggregation. As evidence of this, precipitated NCs are easily resuspended in toluene. Increasing the temperature increases the capping ligand mobility on the surface. At 100 °C (Figure 7A), the NC surface ligands (TOPO) are sufficiently mobile to allow irreversible fusion of neighboring Ni^{2+}:SnO_2 NCs. That fusion is imperfect, generating numerous interfacial grain-boundary defects. We propose that Ni^{2+}:SnO_2 ferromagnetism is activated by these interfacial defects, as summarized phenomenologically in Scheme 2.

Because the surface-capping ligands bind only to Sn^{4+} and not to O^{2-}, the surfaces of the capped NCs must be Sn^{4+} rich and oxygen vacancies (V_O^{n-}) may therefore be the most likely interfacial fusion defects to form. Recently, theoretical models have been proposed that describe how native and charge compensating *n*-type defects in SnO_2 (primarily oxygen vacan-

Scheme 2
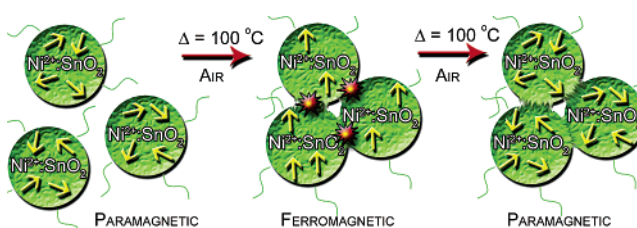
cies, $V_O^{2-,-}$) may activate bound magnetic polarons (BMPs)[1] and, if high enough in concentration, may lead to the formation of ferromagnetic domains.[5,13] In Ni^{2+}:SnO_2, the native defects and charge compensating oxygen vacancies evidently do not play any role in activating ferromagnetism because magnetic ordering is observed only after aggregation of the NCs and not after heating or precipitating the NCs. Because nickel resides in the Ni^{2+} oxidation state, charge compensating oxygen vacancies would be charge neutral (i.e., V_O^0) and therefore would lack the unpaired electrons necessary for mediating magnetic ordering. One scenario consistent with the experimental observations would involve activation of Ni^{2+}:SnO_2 ferromagnetism by V_O^{2-} formed at the NC−NC fusion interfaces. At higher aerobic annealing temperatures or longer aerobic annealing times, these interfacial oxygen vacancies are passivated by atmospheric O_2 or H_2O and stoichiometric SnO_2 is approached, thereby quenching the high-T_C ferromagnetism and returning the material to its paramagnetic phase (Figures 6 and 7, Scheme 2). Strong support for this hypothesis is provided by the observation that deactivation does not occur when the aggregation experiments are performed under inert (N_2) atmospheres (Figure 7B).

D. Activation by Interfacial Fusion Defects as a General Phenomenon. The role of interfacial or grain-boundary defects in activating high-T_C ferromagnetism was first noted in Ni^{2+}:ZnO, where 300 K ferromagnetic saturation moments were shown to correlate with NC aggregate densities formed by room-temperature atmospheric NC aggregation.[17] We have subsequently found this correlation to be general across a broad spectrum of oxide DMSs, including cobalt-doped ZnO[20] and cobalt-doped TiO_2.[18] We have therefore identified a general phenomenological trend in these DMSs, namely that they are paramagnetic as free-standing NCs but exhibit ferromagnetic ordering when aggregated and spin-coated onto fused-silica substrates or when annealed as powders under appropriate conditions that introduce activating lattice defects. Very recently, interfacial defects at SnO_2 DMS thin film−substrate interfaces grown by pulsed laser deposition (PLD)[5] have been postulated to be responsible for the large saturation moments observed in some thin films. It is likely that such lattice defects are more widely influential than currently recognized, and the critical importance of such poorly understood defects is likely in part responsible for the disparate observations often reported for the same materials prepared by different laboratories or by different methods. Experiments are currently underway to explore the role of annealing atmosphere and capping-ligand identity in the thermal activation of high-T_C ferromagnetism in Ni^{2+}:SnO_2 and related oxide DMSs more thoroughly. These experiments should provide a deeper view into the microscopic origins of this intriguing phenomenon.

V. Conclusion

We have developed a new wet chemical preparation of high-quality colloidal Ni^{2+}-doped SnO_2 diluted magnetic semiconductor NCs. Using ligand field electronic absorption, magnetic circular dichroism, and X-ray absorption spectroscopies in tandem with magnetic susceptibility, we showed nickel dopants to be in the Ni^{2+} oxidation state, substituting for Sn^{4+} in a six-coordinate D_{2h} geometry. This oxidation state and coordination geometry remain unchanged when the NCs are spin-coated into films and annealed for short times at low temperatures, despite the fact that the films show robust high-T_C ferromagnetism. The observed ferromagnetic saturation moments, M_s(300 K) = 0.8 μ_B/Ni^{2+}, are indisputably attributable to the presence of Ni^{2+} in the SnO_2 lattice. On the basis of a systematic investigation of the paramagnetic−ferromagnetic magnetic phase transition, the mechanism for activation of ferromagnetism is concluded to involve the formation of nonstoichiometric lattice defects at NC−NC fusion interfaces. These defects were shown to be easily passivated under aerobic conditions, thereby quenching ferromagnetism, but were not passivated under analogous inert atmosphere conditions, leading to assignment of the key defects as interfacial oxygen vacancies ($V_O^{2-,\cdot-}$).

From a practical standpoint, the demonstration that it is possible to complement the favorable semiconducting and optical properties of SnO_2 with strong high-T_C ferromagnetism by introducing Ni^{2+} dopants presents Ni^{2+}:SnO_2 as a promising new candidate for high-temperature spintronics applications. The facile reversibility of the ferromagnetic−paramagnetic phase transition (Figure 7) suggests that reversible ferromagnetic ordering in Ni^{2+}:SnO_2 by even softer chemical or physical perturbations could lead to tunable, real-time control of this ferromagnetism, as well as to a deeper understanding of its microscopic origins.

Supporting Information Available: Low- and high-resolution SEM images and additional magnetic data (three figures). This material is available free of charge via the Internet at http://pubs.acs.org.

JA054205P